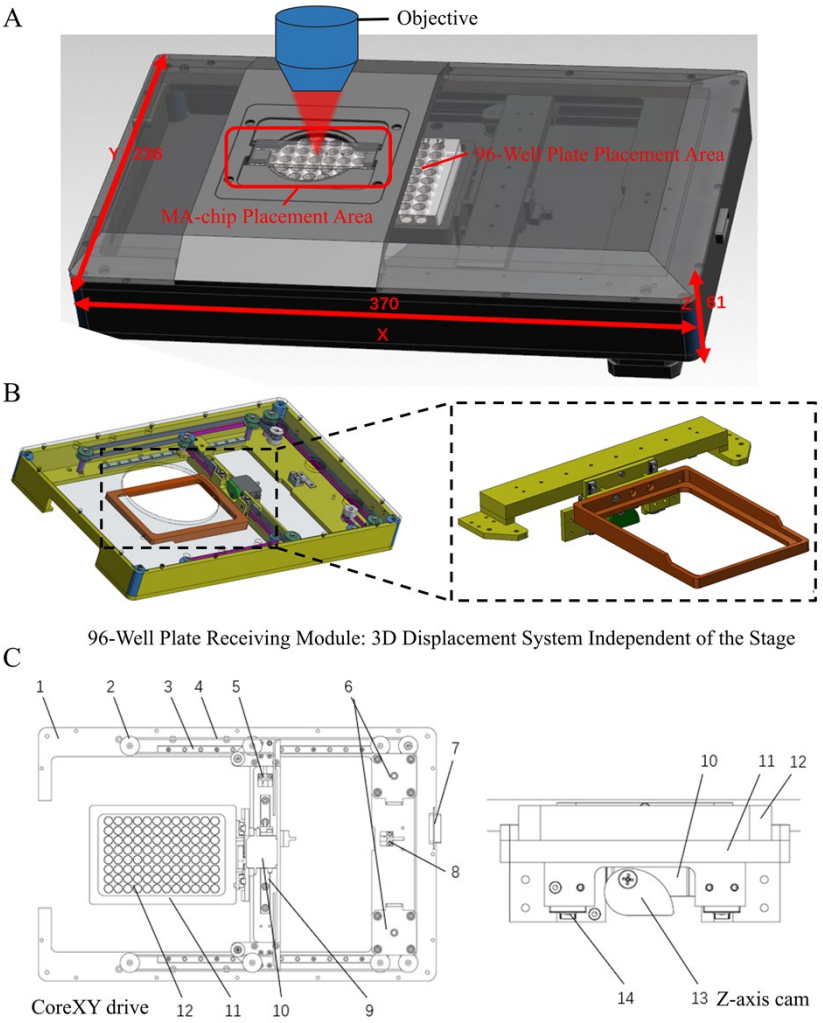

Fig. S1 Mechanical design and automated positioning systems of the OTMA platform. (A) 3D CAD overview of the main motorized three-axis translation stage. The stage provides precise spatial positioning (step resolution: 0.397 µm) of the MA-chip relative to the strictly stationary objective lens (optical trap). (B) Detailed 3D rendering of the custom-built 96-well plate receiver module. This module functions as an independent 3D displacement system integrated below the main stage. (C) 2D schematics illustrating the internal transmission mechanisms of the receiver module. A CoreXY drive architecture governs planar (X-Y) spatial positioning, while a specialized servo-driven cam mechanism (label 13) executes independent Z-axis lifting during droplet collection. This decoupled mechanical design ensures that macroscopic droplet-dispensing actuations do not perturb the high-precision optical trapping operations.

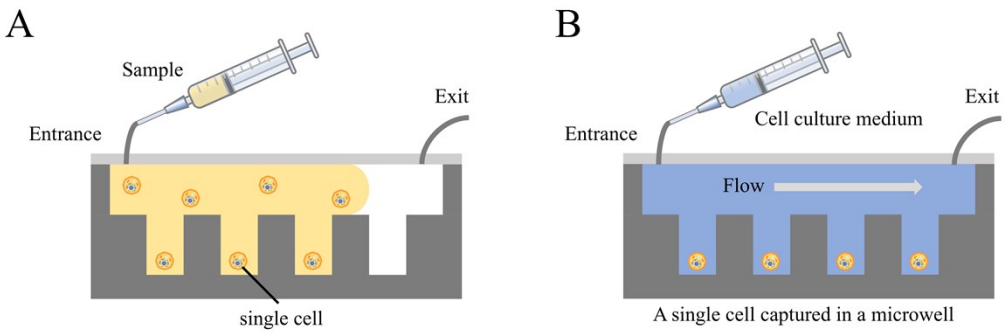

Fig. S2 Schematic illustration of the vacuum-assisted cell loading and hydrodynamic purification workflow. (A) Sample loading: Utilizing the localized negative pressure potential generated by prior degassing of the PDMS matrix (30 min), the cell suspension is introduced into the inlet. The combined effects of the degas-driven flow and gravitational sedimentation facilitate the rapid capture of cells within the microwell array. (B) Background clearance: Continuous perfusion of fresh culture medium (at a flow velocity of 2×10^{-3} m s^{-1} for 10 min) generates a hydrodynamic shear flow within the main channel. This step effectively dislodges and flushes away excess cells loosely adhered to the channel surfaces, while target cells remain stably confined within the shear-sheltered microwells, ensuring a high-purity background for precise optical sorting.

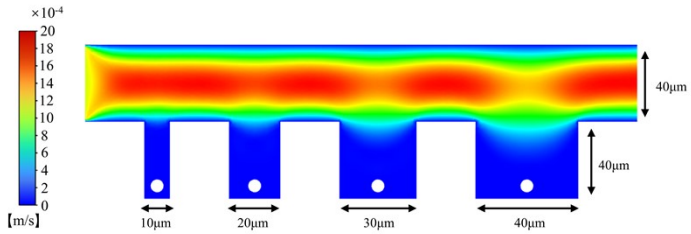

Fig. S3 CFD analysis of the impact of microwell aspect ratio on hydrodynamic shielding. The simulation investigates flow stability within microwells of a fixed depth (40 μm) and varying diameters (10, 20, 30, and 40 μm), corresponding to decreasing aspect ratios (depth-to-diameter) of 4.0, 2.0, ~1.3, and 1.0, respectively. The continuous inlet flow velocity was set to 2×10^{-3} m s^{-1}. The velocity magnitude contours demonstrate that as the microwell diameter increases (i.e., the aspect ratio decreases), the high-velocity laminar flow from the main channel penetrates progressively deeper into the cavity. This enhanced "shear flow penetration" at lower aspect ratios destabilizes the quiescent fluid microenvironment at the bottom, confirming that a sufficiently high aspect ratio (e.g., the unified AR of 1.5 utilized in our MA-chip) is critical for shielding trapped cells from fluidic washout.

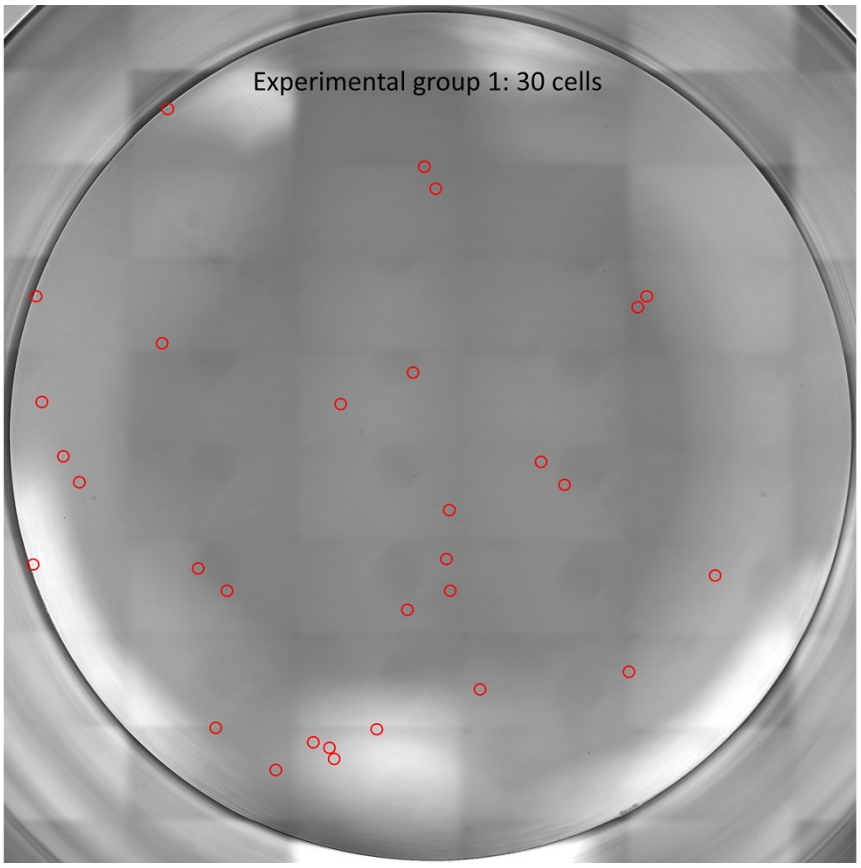
Experimental group 1: 30 cells

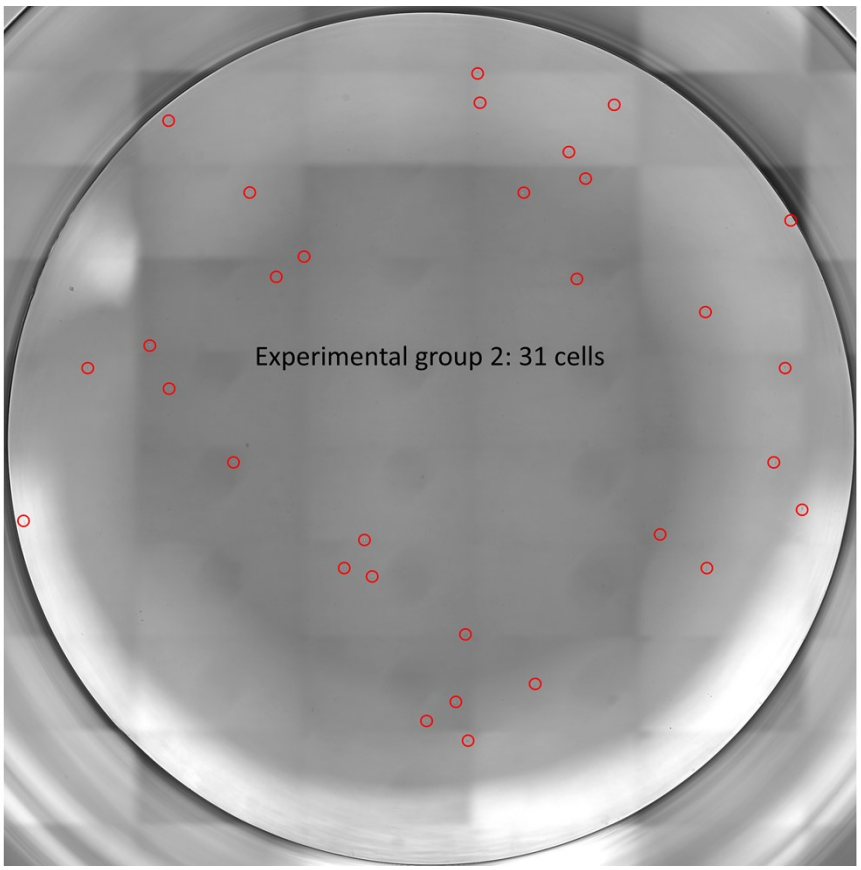
Experimental group 2: 31 cells

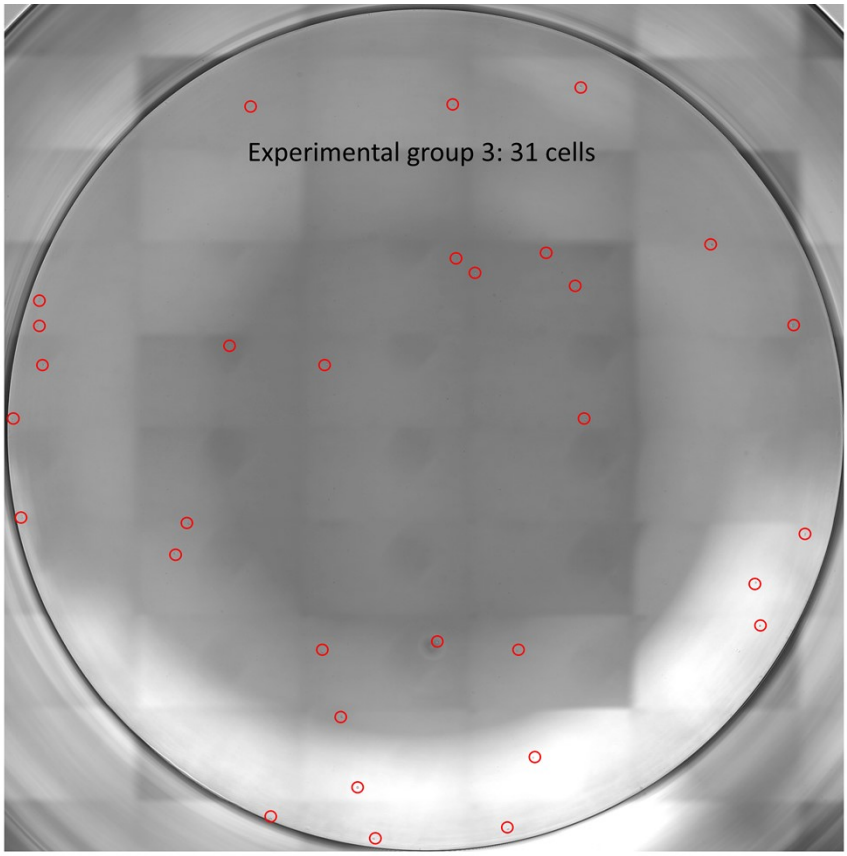

Fig. S4 Quantitative validation of deterministic retrieval efficiency. To verify the system's capability for lossless sample recovery, a defined cohort of 30 target PC-9 cells was sequentially sorted into a single receiving well across three independent biological replicates. Composite whole-well micrographs visualize the spatial distribution of the collected cells across the three trials, with each individual cell highlighted by a red circle. Post-sorting enumeration revealed actual cell counts of 30, 31, and 31, respectively. These results confirm a retrieval efficiency of ≥100%, demonstrating that no target cells were lost during hydrodynamic transport. The marginal surplus observed in two trials is attributable to rare carryover events of residual cells loosely adhered within the microfluidic channel or capillary interface.

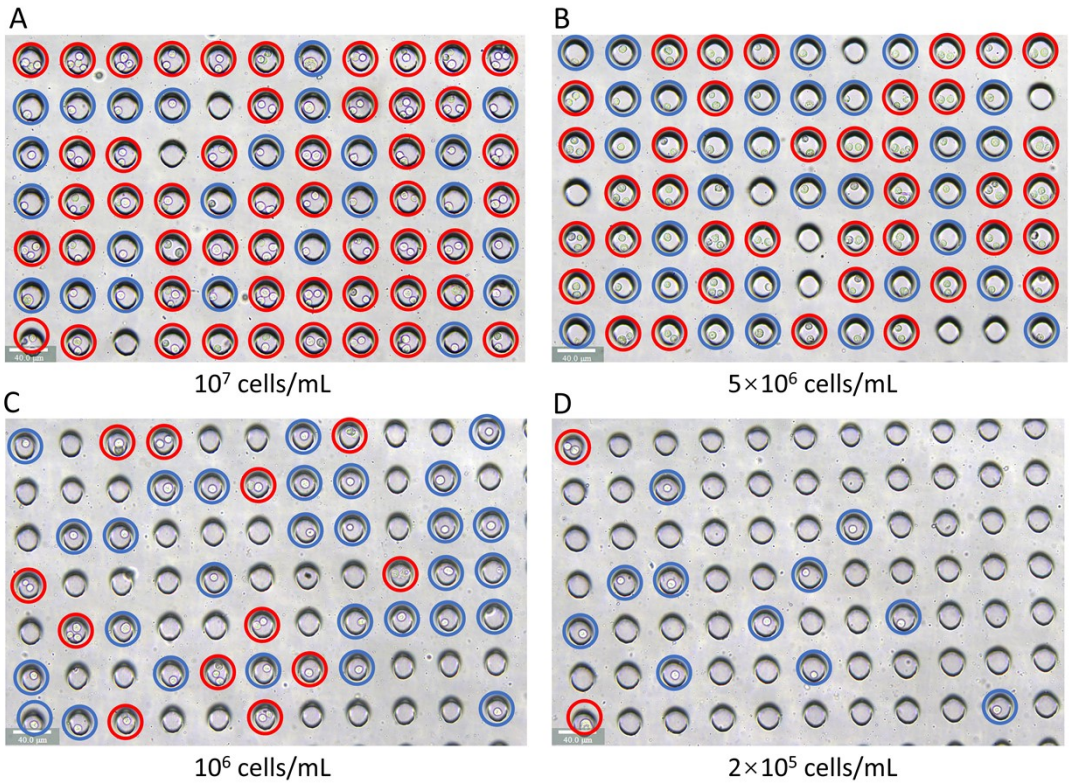

Fig. S5 Representative microscopic images of cell capture in the MA-chip across varying loading concentrations. To visually corroborate the capture statistics governed by the Poisson distribution, PC-9 cells were loaded at concentrations of (A) 10^7, (B) 5×10^6, (C) 10^6, and (D) 2×10^5 cells mL^{-1}. Images shown are representative fields of view selected from three independent biological replicates. Red circles indicate microwells with multiple-cell entrapment, which dominates at excessively high concentrations (e.g., panels A and B). Blue circles indicate ideal single-cell occupancy, which is optimal at the selected working concentration of 10^6 cells mL^{-1} (C). Unmarked wells represent empty capturing sites resulting from low cell density (D). Scale bars: 40 µm.